Boundary-Layer Meteorology (2023) 189:53–76
https://doi.org/10.1007/s10546-023-00825-x

RESEARCH ARTICLE

# The Atmospheric Boundary Layer Above the Marginal Ice Zone: Scaling, Surface Fluxes, and Secondary Circulations

**Joseph Fogarty**[1] · **Elie Bou-Zeid**[1]

Received: 26 December 2022 / Accepted: 20 July 2023 / Published online: 21 August 2023


**Abstract**
The Arctic is undergoing rapid changes due to global warming, including the expansion of the marginal ice zone (MIZ), a zone of mixed ice and open water surfaces. To predict the atmospheric interaction with these surfaces, a critical process in climate models, this paper examines a simplified theoretical framework to non-dimensionalize the dynamics of the atmospheric boundary layer (ABL) over a mixed ice-water surface (MIZ–ABL). A heterogeneity Richardson number, $\mathrm{Ri}_h$, is proposed to account for the difference in temperature between the ice and water surface in relation to the synoptic pressure gradient forcing. With the wind angle relative to the ice-water interface, $\alpha$, this framework hypothesizes that these two dimensionless numbers, regardless of individual dimensional variables (surface temperature and geostrophic wind speed) are sufficient to predict the MIZ–ABL dynamics. To test this framework, large-eddy simulations were employed over half-ice and half-water surfaces, with varying surface temperatures and geostrophic wind velocities. While the surface heat fluxes over ice, water, and the aggregate surface seem to be captured reasonably well by $\alpha$ and $\mathrm{Ri}_h$, the mean wind and turbulent kinetic energy (TKE) profiles were not, suggesting that not only the difference in stability between the two surface, but also the individual stabilities over each surface influence the dynamics. The wind angle had a significant impact on the results, both in terms of heat fluxes at the surface, turbulent and dispersive fluxes in the MIZ–ABL, and the structure of the secondary circulations. When wind blows perpendicular to the water-ice interface, internal boundary layers are favoured except at the highest $\mathrm{Ri}_h$ simulated. For cases with wind parallel to the interface, large rolls parallel to the shore emerge. The paper raises at least as many questions as it answers, highlighting the need for further studies of the MIZ–ABL.

**Keywords** Heterogeneity · Polar boundary layer · Scaling · Sea ice · Secondary circulations

✉ Joseph Fogarty
jf38@princeton.edu

Elie Bou-Zeid
ebouzeid@princeton.edu

[1] Princeton University, Princeton, USA

## 1 Introduction

The polar sea ice surface, a sensitive indicator of global climate change, becomes a sequence of ice and water patches in the fringe zone that separates it from the open ocean. In this "marginal ice zone" (MIZ), the sizes and organization of ice patches (floes) and water patches are influenced by winds, sea currents, and waves, as well as by the thermal exchanges between the air, water, and ice. The ice fraction $f_i$ in that zone is between 15% and 80% (Strong et al. 2017); however, what makes polar surfaces unique is that the near-surface air temperatures may fall in between the surface temperatures of the ice and water, resulting in abrupt spatial transitions between stabilizing and destabilizing surface buoyancy fluxes that produce drastically different turbulence-mean equilibria and time scales (Allouche et al. 2021). Such transitions challenge many of the assumptions usually used in developing parameterizations for turbulent surface-air exchanges and vertical fluxes in the atmospheric boundary layer (ABL), especially homogeneity and equilibrium (Bou-Zeid et al. 2020). This may explain why climate model ensembles generally underpredict sea ice loss rate in the Arctic, and why this underprediction has persisted throughout the last three Intergovernmental Panel on Climate Change (IPCC) model development cycles (Stroeve et al. 2007; Rosenblum and Eisenman 2016). Such uncertainty in climate models' ability to predict sea ice dynamics hinders effective action and decision-making. With the rapidly evolving yearly dynamics of sea ice due to polar amplification now observable in both the Arctic and Antarctic, improving our understanding of the small scale flow dynamics in the MIZ and their coarse scale parameterizations will thus be increasingly critical for predicting and adapting to the now unavoidable impacts of climate change.

Previous studies have analyzed the atmosphere over sea ice surfaces in an attempt to quantify surface fluxes using either observational methods (Lüpkes and Birnbaum 2005; Fiedler et al. 2010; Raddatz et al. 2015) or numerical techniques (Vihma 1995; Wenta and Herman 2019). However, a scaling approach has yet to be established to develop a similarity theory and a set of relevant non-dimensional parameters for the atmospheric boundary layer (ABL) over the marginal ice zone (MIZ–ABL), describing its dynamics and thermodynamics in a generalizable manner. Such a framework might lend some insight as to why current climate models underpredict sea ice and offer avenues for improving their predictive skill with improved coupled surface-atmosphere interaction schemes. In many geophysical models, this interaction is essential to predict future states of the environment. The most widely-used scheme remains the Monin-Obukhov similarity theory (MOST). MOST is known to have serious limitations under stable conditions over continuous ice or snow surfaces (Bou-Zeid et al. 2010; Allouche et al. 2022). Another consequential limitation of MOST is that it operates under the assumption of spatial homogeneity and production-dissipation equilibrium (see Townsend (1961), Bradshaw and Huang (1995), Zahn et al. (2023)), which are clearly violated for the ABL over the MIZ.

Heterogeneity in the MIZ causes multiple transitions in the surface boundary conditions that influence surface fluxes, the mean flow, and turbulence. Locally, turbulence statistics may no longer be in quasi-equilibrium with the mean state (Momen and Bou-Zeid 2017; Mahrt and Bou-Zeid 2020), and the often-assumed near balance between turbulence production and dissipation may not hold. Such conditions are generally found to intensify the surface exchanges of heat, momentum, and trace chemicals (Bates et al. 2006; Bou-Zeid et al. 2007; Esau 2007). These modified surface exchanges propagate through the atmosphere, which can influence cloud formation and radiative feedbacks to the sea ice surface (Khvorostyanov et al. 2003; Palm et al. 2010; Liu et al. 2012). Therefore, modelled surface fluxes in the MIZ–ABL

need to be particularly accurate to avoid feedbacks that can drift the model state far from physical reality (Pithan et al. 2016).

Unfortunately, surface fluxes remain poorly understood and represented in models (Bourassa et al. 2013). A long-standing challenge here is how to represent surface heterogeneity that is not resolved by the model grid (Bou-Zeid et al. 2020). For example, surface patterns, which drive fluxes via ice-water temperature differences, are rarely taken into account (Taylor et al. 2018). Another is the aforementioned lack of a dimensionless approach that allows generalizable conclusions. Some recent efforts to develop such a non-dimensional framework for heterogeneous surfaces have been made (Omidvar et al. 2020; Margairaz et al. 2020; Morrison et al. 2021), but are yet to be tested over the MIZ. To begin addressing these gaps in current literature, this study will answer the following questions:

1. What scaling can capture the competing effects of buoyant circulations and synoptic forcing to provide a unifying framework for understanding the dynamics and thermodynamics of the heterogeneous MIZ–ABL?
2. How do the mean wind profile, turbulent kinetic energy (TKE), and surface fluxes respond to an increase in the surface temperature difference $\Delta\theta_0$ between ice and water?
3. What is the effect of the orientation of the surface patterns relative to the wind direction $\alpha$?
4. How do $\Delta\theta_0$ and $\alpha$ combine to set up secondary circulations and modulate the turbulent and dispersive heat and momentum exchanges in the MIZ–ABL?

These questions thus focus on the buoyancy dynamics versus wind speed and angle effects. The equally-important influence of patch scale and realistic ice-water patterns are also being investigated, but we intend to report them in a separate study.

Section 2 constructs a framework to analyze these questions, while proposing a scaling for important parameters such as heat flux and wind velocity. The remaining questions will be answered using large-eddy simulations (LES) of the MIZ–ABL over different idealized surfaces; the numerics and domain set-up are detailed in Sect. 3. The first suite of simulations, Suite I, changes external parameters such as the difference in surface temperatures $\Delta\theta_0$ and geostrophic velocity $M_g$, but keeps the wind direction constant. This suite is analyzed to focus on the competing effect of buoyancy and geostrophic forcing in Sect. 4. In Suite II, the geostrophic wind speed is kept constant to focus on the effect of changes in geostrophic wind direction and surface temperature contrasts (Sect. 5). Suite II is also used to examine the secondary circulations and how they change with surface and geostrophic forcings in Sect. 6, before concluding in Sect. 7 with the answers to the motivating questions.

## 2 Theoretical Background and Dimensional Analysis

There are at least seven different variables (not including $\alpha$, the dimensionless wind angle) that are important when considering an MIZ–ABL over a heterogeneous sea ice surface with two patch types: ice and water (this excludes the common presence of melt ponds on top of the ice). The four length scales are the MIZ–ABL depth $z_i$, the roughness lengths of the two different surfaces $z_{01}$ and $z_{02}$, and the characteristic heterogeneity length scale $l_h$ (floe or water patch scale). One important velocity scale is $M_g$, the geostrophic wind velocity. Other relevant parameters include the Coriolis frequency $f_c$, and the buoyancy scale based on the surface temperature difference, $\frac{g}{\theta_r}\Delta\theta_0$, where $g$ is the acceleration of gravity, and $\theta_r$ is some reference temperature. $\Delta\theta_0$ is the (positive) temperature difference between the two surfaces, that is, $\Delta\theta_0 = \theta_w - \theta_i$, where $\theta_w$ is the surface temperature of the ocean and $\theta_i$

is the surface temperature of the ice. These seven variables involve two dimensions (length and time); invoking Buckingham-$\Pi$ theorem then yields $7-2=5$ dimensionless $\Pi$ groups. Including the wind angle then results in six total dimensionless $\Pi$ groups. In this study, we select the following non-dimensional combinations:

$$\Pi_1 = \alpha \qquad \Pi_2 = \frac{g}{\theta_r}\frac{\Delta\theta_0}{M_g^2/z_i} = \mathrm{Ri}_h, \tag{1}$$

$$\Pi_3 = \frac{M_g}{z_i f_c} = \mathrm{Ro} \qquad \Pi_4 = \frac{l_h}{z_i}, \tag{2}$$

$$\Pi_5 = \frac{z_{01}}{z_i} \qquad \Pi_6 = \frac{z_{02}}{z_{01}}. \tag{3}$$

The focus of this study is on the first two non-dimensional groups; $\Pi_1$, which represents the geostrophic wind angle relative to surface heterogeneity patterns, and $\Pi_2 = \mathrm{Ri}_h$, a modified Richardson number that represents the ratio of buoyancy generated by the heterogeneous surfaces to inertia generated by the mean wind (Omidvar et al. 2020; Margairaz et al. 2020). Our formulation of $\mathrm{Ri}_h$ uses a temperature difference and $z_i$ as a length scale, similar to the thermal heterogeneity parameter proposed in Margairaz et al. (2020) but with the heterogeneity length scale; the two are thus identical given a fixed $z_i/l_h$. $\Pi_3 = \mathrm{Ro}$ represents the classic Rossby number, which will remain constant in these simulations since it has an important but often neglected impact on mean profiles in the ABL (Ghannam and Bou-Zeid 2021); however, its dimensional inputs $M_g$ and $f_c$ may vary. The remaining $\Pi$ groups all represent geometric ratios. The $\Pi_4$ group represents the ratio of the two integral scales $l_h$ and $z_i$, capturing the patch scale relative to the turbulent integral scale dictated by $z_i$. The ratio of surface roughness to integral scales is represented by $\Pi_5$; it encodes the scale separation related to the effective Reynolds number of the simulations that we will detail later. The ratio of the two roughness length scales, $z_{01}$ and $z_{02}$, is represented by $\Pi_6$; it can also result in secondary circulations due to stress divergence (Willingham et al. 2014; Anderson et al. 2015; Bou-Zeid et al. 2020). While these geometric ratios are quite important, they will be maintained constant in this study to focus on the dynamical ratios $\Pi_1$ and $\Pi_2$. Specifically, in our simulations, $\Pi_6 = 1$, meaning that $z_{01} = z_{02} = 0.5$ cm so as to only analyze the effect of surface temperature differences via $\Delta\theta_0$ on the flow (and since ice and water roughness lengths vary with the surface state, but are not usually drastically different at low wind speeds, see Untersteiner and Badgley (1965) and Brutsaert (2005)).

In these simulations, $\Pi_4$, and the heterogeneity scale $l_h$ in general, is also not to be considered. The simulations are idealized in the sense that, however $l_h$ is defined, we maintain a half-ice and half-water surface ratio with a striped pattern. The focus will mainly be on either the surface temperature contrast or geostrophic wind in the context of the entire flow, and in the limit of surface patches that are larger by an order of magnitude or more than the ABL depth. These domain set-ups are idealized yet horizontally periodic, as will be detailed later, to facilitate the testing of scaling approaches and to elucidate the largest-scale circulations that can develop at the ice-water edge. This is not to say that $\Pi_4$ is not important; however, since $l_h$ may be a function of many variables and since one single parameter to quantify heterogeneity may not be sufficient to capture the full flow field, we elect to leave its detailed analysis to future studies of more chaotic patterns.

The $\Pi_2$ group, $\mathrm{Ri}_h$, is very important in scaling both the dynamics and thermodynamics of the flow. This group can be written as:

$$\mathrm{Ri}_h = \frac{W_b^2}{M_g^2}, \tag{4}$$

where $W_b$ is a buoyancy velocity scale, defined as:

$$W_b = \sqrt{\frac{g}{\theta_r} \Delta\theta_0 z_i} \,. \tag{5}$$

Thus, $\mathrm{Ri}_h$ measures whether the geostrophic advective forcing or the buoyant thermal forcing dominate the dynamics. It also indicates that the air velocity and turbulence parameters may scale with either of these velocity scales, or a mixed one, depending on the dominant forcing as we will elucidate later.

However, to understand thermodynamic surface-atmosphere interactions, a variable of interest for prediction is the surface heat flux $\langle \overline{H} \rangle$ (where the overbar denotes Reynolds averaging in time and the $y$-direction, and the angled brackets denote averaging in $x$ over the whole domain, or over ice or water separately when a subscript $i$ or $w$ is added). In an attempt to relate $\langle \overline{H} \rangle$ to $\mathrm{Ri}_h$, two specific buoyancy velocity scales, one for the whole ice surface and one for the whole water surface, can also be formulated as:

$$W_{b,i} = \sqrt{\frac{g}{\theta_r}(\theta_a - \theta_i) z_i} \,, \quad W_{b,w} = \sqrt{\frac{g}{\theta_r}(\theta_w - \theta_a) z_i} \,, \tag{6}$$

where $\theta_a$ is a bulk air temperature and $\theta_w > \theta_a > \theta_i$. The use of a buoyancy velocity scale over the ice surface is justified by the fact that the heat flux over the ice is modulated by the secondary flow that is setup over the entire domain, driven jointly by the ice and water surfaces and their thermal contrast. This 'mixed' buoyant flow is thus represented by our choice of $W_b$ (Eq. 5), a function of the temperature difference of both surfaces. We can relate these values in Eq. 6 to the bulk buoyancy velocity $W_b$ by some constants $a_i$ and $a_w$, such that:

$$W_{b,i} = a_i W_b \,, \quad W_{b,w} = a_w W_b \,, \tag{7}$$

and then infer the constants accordingly as:

$$a_i = \sqrt{\frac{\theta_a - \theta_i}{\Delta\theta_0}} \,, \quad a_w = \sqrt{\frac{\theta_w - \theta_a}{\Delta\theta_0}} \,. \tag{8}$$

Now, consider the average heat flux over an MIZ region; it scales like $H \sim V \Delta\Theta$, where $V$ is some exchange velocity scale and $\Delta\Theta$ is some difference in temperature that drives the flux. The velocity scale $V$ could be replaced by $M_g$, $W_b$, or some combination $(m M_g + n W_b)$ thereof. If the surface is statistically homogeneous over some large area such that the air temperature is mainly dictated by the two surface temperatures, the $\Delta\Theta$ in the scaling can be replaced by the surface temperature contrast $\Delta\theta_0$. Using Eq. 5, the average heat flux in the MIZ–ABL could then be formulated as:

$$H \sim (m M_g + n W_b) \left( \frac{\theta_r}{g z_i} W_b^2 \right) . \tag{9}$$

However, if we were to consider the heat flux over ice only, we would replace the second $W_b$ in the above equation (which represents the driving air-surface thermal difference) with $W_{b,i}$ yielding:

$$H_i \sim \frac{\theta_r}{g z_i} (m M_g + n W_b) W_{b,i}^2 \,, \tag{10}$$

with the combination $(m M_g + n W_b)$ staying unchanged because this velocity reflects the larger circulation and turbulence state in the MIZ–ABL (although, as we will note later, the coefficients might vary in space). From Eq. 8, we can come back into $W_b$ terms by writing:

$$H_i \sim a_i^2 \frac{\theta_r}{g z_i} (m M_g + n W_b) W_b^2 \,, \tag{11}$$

which can be expressed in terms of the heterogeneity Richardson number from Eq. 4 (and absorbing the proportionality constant into $m$):

$$H_i = a_i^2 \frac{\theta_r}{g z_i} M_g^3 m \left(1 + \frac{n}{m} Ri_h^{1/2}\right) Ri_h \,. \tag{12}$$

Following the same derivation, but allowing for potentially different coefficients in the mixed velocity scale, the heat flux over the water surface can be written as:

$$H_w = a_w^2 \frac{\theta_r}{g z_i} M_g^3 p \left(1 + \frac{q}{p} Ri_h^{1/2}\right) Ri_h \,. \tag{13}$$

The coefficients $m$ and $p$ are the proportionality constants needed to model the fluxes, while the ratios $n/m$ and $q/p$ essentially act to change the relative influence of $M_g$ and $W_b$ in the mixed velocity scale. Since $H_i$ is a physically negative quantity, we expect the value of $m$ to always be negative (since it absorbs the proportionality constant), while the value of $p$ should always to be positive.

## 3 Large-Eddy Simulations

Large-eddy simulations (LES) are widely used to model heterogeneous high Reynolds number flows (Baidya Roy 2002; Bou-Zeid et al. 2004; Courault et al. 2007; Huang et al. 2011; Maronga and Raasch 2013; Stoll et al. 2020), including the MIZ–ABL. Unlike a direct numerical simulation (DNS), an LES is able to attain the Reynolds number of the MIZ–ABL ($\mathrm{Re} \sim 10^7$), because the smaller turbulent eddies (smaller than the grid or filter size, which is equivalent to the numerical grid spacing in our simulations) are not explicitly resolved. However, large turbulent eddies, the heterogeneity of the surface, the advective fluxes (but not the leading edges of developing internal boundary layers), and the large-scale ice patterns are captured, making this a computationally and physically appealing approach. By retaining these larger structures, most of the turbulent energy and fluxes are explicitly resolved, allowing for investigation of three-dimensional flow structures that may arise over these heterogeneous surfaces.

In this study, the incompressible filtered Navier–Stokes equations (with the Boussinesq approximation for the mean state) and heat budget are solved for a horizontally periodic flow, representing the dynamics of turbulent scales larger than the grid:

$$\frac{\partial \widetilde{u}_i}{\partial x_i} = 0 \,, \tag{14}$$

$$\frac{\partial \widetilde{u}_i}{\partial t} + \widetilde{u}_j \frac{\partial \widetilde{u}_i}{\partial x_j} = -\frac{1}{\rho_r} \frac{\partial p}{\partial x_j} + \widetilde{F}_i + f_c \epsilon_{ij3} \widetilde{u}_j - g \delta_{i3} \left(1 - \frac{\hat{\theta}}{\theta_r}\right) - \frac{\partial \tau_{ij}}{\partial x_j} \,, \tag{15}$$

$$\frac{\partial \widetilde{\theta}}{\partial t} + \widetilde{u}_j \frac{\partial \widetilde{\theta}}{\partial x_j} = -\frac{\partial q_j}{\partial x_j} \,. \tag{16}$$

In the equations above, $i$ is the free index and $j$ the repeated index invoking the Einstein summation rule; $u_i$ is the velocity vector; $x_i$ is the position vector; $p$ is a modified pressure (see Bou-Zeid et al. (2005) for details); $\theta$ is the potential temperature; $\theta_r$ and $\hat{\theta}$ are the Boussinesq reference (planar mean in our calculations) and the perturbation from that reference for potential temperature; $\rho_r$ is the reference mean density corresponding to $\theta_r$; and $F_i$ is the

main flow-driving force (a synoptic pressure gradient). The Coriolis force is represented by the third term on the right-hand side of Eq. 15, with $f_c$ being the Coriolis parameter and $\epsilon_{ij3}$ representing the Levi-Civita symbol. Gravity and buoyancy are represented by the fourth term on the right-hand side of Eq. 15, where $\delta_{ij}$ is the Kronecker delta. Any variable with a tilde represents a quantity filtered via the numerical grid spacing $\Delta$. The only explicit filtering needed is at scales $2\Delta$ and $4\Delta$ to compute the dynamic Smagorinsky constant $c_s$ and at a scale $2\Delta$ for the local wall model; for these we use a sharp-spectral cutoff filter. As noted before, an overbar denotes averaging in time and in $y$, used as a surrogate for ensemble Reynolds averaging, while spatial averaging over the heterogeneous domain in $x$ will be denoted by angled brackets. The subgrid scale stress $\tau_{ij} = \widetilde{u_i u_j} - \widetilde{u}_i \widetilde{u}_j$ and buoyancy flux $q_j = \widetilde{u_j \theta} - \widetilde{u}_j \widetilde{\theta}$, which result from the filtering, are modelled using a Lagrangian scale-dependent dynamic model (Bou-Zeid et al. 2005) with a constant subgrid scale Prandtl number of 0.4. This model was validated for boundary layer flows over both homogeneous and heterogeneous terrain by reproducing experimental velocity and stress profiles obtained by Bradley (1968) after a change in surface roughness. It was then further validated for urban flows (Tseng et al. 2006; Li et al. 2016), and both stable and unstable boundary layers (Kleissl et al. 2006; Kumar et al. 2006; Huang and Bou-Zeid 2013). Therefore, the ability of this model to successfully capture the impacts of stability and spatial transitions in surface properties will not be tested further in this study.

The LES employs boundary conditions that are periodic in the horizontal, with zero vertical velocity at the top and bottom of the domain, as well as a stress-free top lid ($\partial_z u_i = 0$ where $i = 1, 2$), with zero heat flux. These mimic a very strong top inversion, and are adequate for our set-up since the top of the domain is not stably stratified and there is thus no need for a sponge to avoid wave reflection. This allows for the surface characteristics to be isolated from $z_i$ and the inversion strength. The indices $i = 1, 2, 3$ represent the $x$, $y$, and $z$ directions, oriented along the streamwise, cross-stream, and vertical directions, respectively. At the bottom of the domain, the surface stress and heat flux are computed by a wall model based on a local law-of-the-wall formulation (Bou-Zeid et al. 2005), with Monin-Obukhov buoyancy correction. Numerically, a pseudo-spectral approach is employed in the horizontal, and an explicit second-order centred difference scheme used in the vertical. Time advancement is done using the fully explicit second-order Adams-Bashforth scheme. Dealiasing of the convective terms is performed using the 3/2 rule (Orszag 1971). Pressure is computed from a Poisson equation obtained by applying the incompressibility assumption and setting the divergence of the momentum to zero. The base-case Coriolis force is equivalent to one at the latitude of $\Phi = 90°$ N (but changed to keep $Ro$ constant). See Table 1 for more details on the LES set-up.

The LES is used to model MIZ–ABL flow over 10 km $\times$ 10 km patterns of idealized ice/water surfaces, where one bottom node represents either water or sea ice. For these simulations, half of the domain will be ice, and the other half will be a water surface. From a birds-eye view, these look like two semi-infinite interface heterogeneity (or meso-$\alpha$ heterogeneity, as depicted in Figure 1 in Bou-Zeid et al. (2020)). However, due to the periodicity of the domain, this picture only applies near the surface layer. Here, if there is a perpendicular flow going from ice to water, the internal equilibrium layer (IEL, defined as the layer where the air has reached complete equilibrium with the underlying surface) has had enough time to grow to some height $\sim l_h/100 \sim 50$ m by the time the flow reaches the ice patch again. However, the dynamics of the internal boundary layer (where the flow has felt the new surface underneath but did not yet equilibrate with it, and which grows to some height $\sim l_h/10 \sim 500$ m) and outer layer aloft may not have equilibrated yet, which properly

**Table 1** Large-Eddy simulation numerical details (valid for all simulations in this paper)

| | |
|---|---|
| Domain height, $z_i$ | 1 km |
| Horizontal domain size, $L_x \times L_y$ | 10 km × 10 km |
| Number of grid points ($N_x$, $N_y$, $N_z$) | (200, 200, 100) $\approx 4 \times 10^6$ points |
| Vertical mesh spacing, $dz$ | 10 m |
| Horizontal mesh spacing, $dx$, $dy$ | 50 m |
| Initial air temperature $\theta_{a,0}$ | $\theta_{a,0} = 0.4\theta_w + 0.6\theta_i$, constant profile |
| Warm up period | 2 inertial periods ($4\pi/f_c$) |
| Simulation time step | 0.05 s |
| Averaging period | 1 inertial period ($2\pi/f_c$) |
| Frequency of statistical sampling | 100 timesteps = 5 s |
| Frequency of statistics output | 20000 timesteps = 1000 s |

Time is represented in terms of inertial periods, $2\pi/f_c$, which is the time scale associated with the response of the mean flow since it represents the Coriolis redistribution of energy between $u$ and $v$ (Momen and Bou-Zeid 2016)

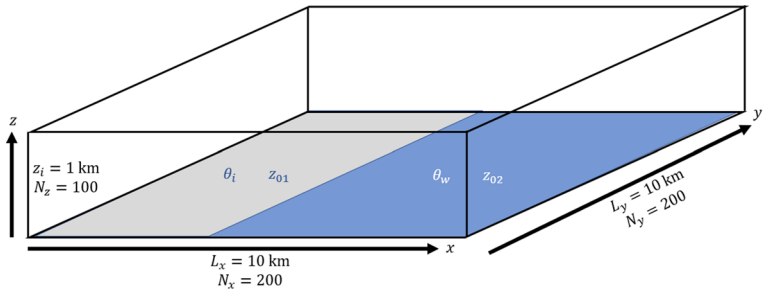


**Fig. 1** Schematic of the large-eddy simulation domain set-up. The ice has a surface temperature of $\theta_i$ and roughness length $z_{01}$; the water surface has $\theta_w$ and $z_{02}$, though here we use $z_{01} = z_{02}$

represents sea ice patterns of this scale in the polar MIZ (due to commonly-seen leads and polynyas, see Claussen (1991)) (Fig. 1).

## 4 Scaling at Increasing Heterogeneity Richardson Number

To understand how key flow variables (mean velocities, fluxes) scale as $Ri_h$ (the $\Pi_2$ group) increases, we first designed a suite of simulations to determine if that number is sufficient to describe the impact of the balance between mean wind and buoyancy contrast on the flow. This is done by conducting simulations with the same $\mathrm{Ri}_h$, but different values of $M_g$ and $\Delta\theta_0$, as in Table 2. Note that this $\mathrm{Ri}_h$ is fundamentally different the classical Richardson number based on vertical stability, where buoyancy dominates when the latter $\ll 1$. The $\mathrm{Ri}_h$ defined here is always positive and represents the competition between synoptic forcing and thermal circulation in modulating the mean flow and fluxes. However, to keep the Rossby number Ro constant when changing $M_g$, the Coriolis frequency $f_c$ must also be changed to keep the Ro constant. This resulted in one Coriolis frequency of $f_c = 2.92 \times 10^{-4}$ that is higher that what occurs anywhere on Earth, but for this scaling analysis this is not a consequential problem

**Table 2** Suite I simulation details (all external variables except $\mathrm{Ri}_f$)

| Simulation | $M_g$ ($\mathrm{m\,s^{-1}}$) | $\Delta\theta_0$ (K) | $\theta_{a,0}$ (K) | $f_c$ (Hz) | $\mathrm{Ri}_h$ | $W_b$ ($\mathrm{m\,s^{-1}}$) | $\mathrm{Ri}_f$ |
|---|---|---|---|---|---|---|---|
| dT02-M01-perp | 1 | 2 | 270.2 | $7.26 \times 10^{-5}$ | 72.6 | 8.1 | 0.120 |
| dT04-M01-perp | 1 | 4 | 270.4 | $7.26 \times 10^{-5}$ | 145.2 | 11.4 | 0.209 |
| dT02-M02-perp | 2 | 2 | 270.2 | $1.46 \times 10^{-4}$ | 18.2 | 8.1 | 0.022 |
| dT04-M02-perp | 2 | 4 | 270.4 | $1.46 \times 10^{-4}$ | 36.3 | 11.4 | 0.028 |
| dT08-M02-perp | 2 | 8 | 270.8 | $1.46 \times 10^{-4}$ | 72.5 | 16.2 | 0.048 |
| dT16-M02-perp | 2 | 16 | 271.6 | $1.46 \times 10^{-4}$ | 144.5 | 22.9 | 0.149 |
| dT08-M04-perp | 4 | 8 | 270.8 | $2.92 \times 10^{-4}$ | 18.1 | 16.2 | 0.021 |
| dT16-M04-perp | 4 | 16 | 271.6 | $2.92 \times 10^{-4}$ | 36.1 | 22.9 | 0.042 |

(one can always reduce all input variables to maintain the same $\Pi$s). All simulations in this suite have a mean wind that is perpendicular to the ice-water edge.

First, we consider the dynamical aspects of the flow. If buoyancy forces were negligible ($\mathrm{Ri}_h \ll 1$), normalizing by $M_g$ should collapse the profiles of $\langle\overline{M}\rangle$ into one, regardless of the $\mathrm{Ri}_h$ value. This is indeed the case for the lowest two $\mathrm{Ri}_h$ simulations, as depicted in Fig. 2a. If the driving pressure gradient represented by $M_g$ were negligible, on the other hand, normalizing these $\langle\overline{M}\rangle$ profiles by $W_b$ would be the right way to collapse all wind profiles together. As seen in Fig. 2b, however, only simulations of similar $\mathrm{Ri}_h$ collapse the wind profiles when scaled with $W_b$. This indicates that under the conditions simulated here (representative of typical temperature contrasts and geostrophic winds in the MIZ, see Hall et al. (2004), Chechin et al. (2019)) buoyancy never dominates the dynamics and the geostrophic forcing remains important. In general, neither of the forcings represented in the heterogeneity Richardson number is dominant across the whole LES suite, which was the intended outcome of the design of this suite of simulations to examine the role of the varying balance between buoyancy and synoptic forcing.

The near collapse of most simulations with similar $\mathrm{Ri}_h$ values, whether normalized by $W_b$ or $M_g$, seem to indicate that the heterogeneity Richardson number is indeed a key dimensionless number for this problem. However, as $\mathrm{Ri}_h$ increases, one can notice that the shapes of the profiles (with similar $\mathrm{Ri}_h$) start to become different and do not collapse with either scaling. In this range, it seems that the buoyancy forces are becoming more important, setting up secondary circulations that do not seem to scale exactly with $\mathrm{Ri}_h$. The most likely explanation is that surface heat fluxes no longer scale linearly with the temperature contrast, and the bulk $\mathrm{Ri}_h$ based on that contrast is no longer sufficient to fully describe the physics (this is further investigated in Sect. 6). One might need to adopt a heat flux contrast-based $\mathrm{Ri}_{f,h}$, or possibly the two heat fluxes or surfaces temperatures of water and ice should be treated as two distinct dimensional inputs requiring an additional $\Pi$ group (an $Ri$ over water and another over ice, as in Omidvar et al. (2020)).

To further examine the consequences of this departure from exact $Ri_h$ scaling, we consider the domain-averaged TKE that provides information on the mixing of the atmosphere and surface-air interactions. As seen in Fig. 3a, normalizing the TKE profiles by $M_g^2$ is not adequate, especially for those simulations with a high $\mathrm{Ri}_h$ (the dotted lines and dot-dash lines). In Fig. 3b, a scaling with $W_b^2$ is tested but it also does not collapse the results onto a single curve. To further investigate, scalings consisting of a mixture of $M_g$ and $W_b$ are attempted (e.g., $aM_g^2 + bW_b^2$ or $M_g^m W_b^n$ where $m + n = 1$ and $a$ and $b$ are some scaling

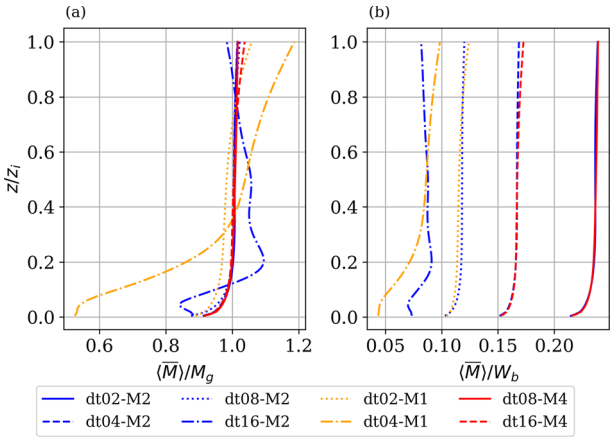


**Fig. 2** **a** Profiles of $\langle \overline{M} \rangle$, normalized by the geostrophic speed $M_g$. Similar line styles correspond to similar values of $\mathrm{Ri}_h$. Similar line colours correspond to equal geostrophic wind speeds. **b** as in **a**, but the profiles are scaled by $W_b$

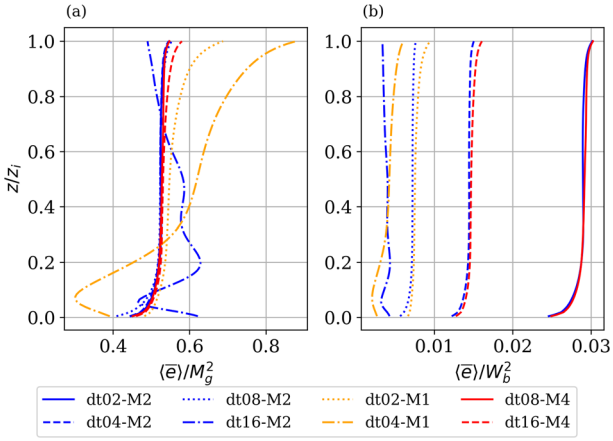


**Fig. 3** **a** Profiles of averaged TKE, $\langle \overline{e} \rangle$, normalized by the square of geostrophic speed $M_g^2$. Similar line styles correspond to similar values of $\mathrm{Ri}_h$. Similar line colours correspond to the equivalent geostrophic wind speeds. **b** as in **a**, but the profiles are scaled by $W_b^2$

constants), but no such combination of scalings provides an adequate way to fully separate these profiles using external parameters (not reported). The hypothesized cause is similar to the one advanced above for the lack of collapse of mean velocity profiles: $Ri_h$ is a necessary but insufficient measure to explain the dynamics of air flow over ice-water mixtures.

We now turn our attention to the scaling of surface sensible heat fluxes, calculated from the LES via the wall model (based on MOST). For the different surface types, different values of $n$, $m$, $q$, and $p$ (see Eqs. 12 and 13) are investigated to find the values that best reproduce the simulated heat fluxes. Setting $m = p = 1$ as a first guess allows for investigation of the ratios $n/m$ and $q/p$ that yield the best linear fit. For the ice surface, the optimal ratio $n/m$ is found to be $-0.25$, with a corresponding $R^2$ value of $-0.971$. We will thus adopt $n_{perp}/m_{perp} = -0.25$ (where the subscript $perp$ refers to those cases where the flow is

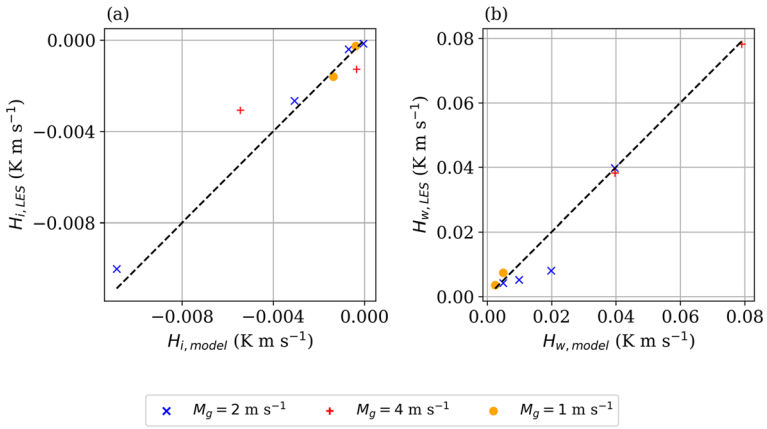


**Fig. 4** **a** Plot of modelled heat flux ($H_{i,model}$, see Eq. 17) versus LES heat flux ($H_{i,LES}$) spatially-averaged over the ice surface for perpendicular wind. Here, $m_{perp} = -2.79 \times 10^{-4}$ and $n_{perp}/m_{perp} = -0.25$. **b** as in **a**, but for the water surface, following Eq. 18, where $p_{perp} = 3.05 \times 10^{-3}$ and $q_{perp}/p_{perp} = 0$

perpendicular to the ice-water edge), which implies a scaling of the heat flux from ice with $\mathrm{Ri}_h$ and $\mathrm{Ri}_h^{3/2}$ (via Eq. 12). The optimal ratio $q_{perp}/p_{perp}$ for modelling $H_w$ is 0, which gives an $R^2$ value of 0.986 and implies no role for $W_b$ in setting the exchange velocity. However, since $W_b$ still sets the air-surface temperature difference, it influences the exchange of heat over water and the resulting dynamics, and it thus appears in the scaling of the heat flux with $\mathrm{Ri}_h$ that results for these perpendicular cases via Eq. 13.

Substituting in these values of the coefficient for ice and water in Eqs. 12 and 13 gives the following relations between an external parameter (which combines the synoptic forcing and the temperature contrast) and the heat flux:

$$H_{i,model} = a_i^2 \frac{\theta_r}{g z_i} M_g^3 m_{perp} \left( \mathrm{Ri}_h - \frac{\mathrm{Ri}_h^{3/2}}{4} \right), \tag{17}$$

$$H_{w,model} = a_w^2 \frac{\theta_r}{g z_i} M_g^3 p_{perp} \mathrm{Ri}_h. \tag{18}$$

The remaining two coefficients, $m_{perp}$ and $p_{perp}$, can now be determined to provide the best modelled heat fluxes compared to the LES determined ones, and we obtain $m_{perp} = -2.79 \times 10^{-4}$ and $p_{perp} = 3.05 \times 10^{-3}$ (these are thus the slopes of the linear regressions for $H_i$ and $H_w$, respectively). The relationship these equations yield is apparent in Fig. 4. The performance of this scaling model for heat fluxes is quite satisfactory and suggests that $Ri_h$ may be sufficient for parameterization of these fluxes, despite its inability to explain the mean wind speed and TKE profiles. Recall from Eq. 8 that the variables $a_i$ and $a_w$ are defined from the surface temperature difference between the two different surfaces ($\Delta\theta_0$) and the difference between the surface and atmospheric temperature. Thus, with the above formulation, one can predict the heat flux over each surface by knowing *a priori* the temperature of the surface, the atmospheric temperature, and geostrophic wind, all of which are available at each time step in a coarse numerical model. The surface temperature contrast does require a model to resolve the surface energy budget of the different patches, at least in a MOSAIC sense (Li et al. 2013), which for the MIZ implies having a sea ice model that distinguishes between the ice and water components and solves for their surface energy budgets individually.

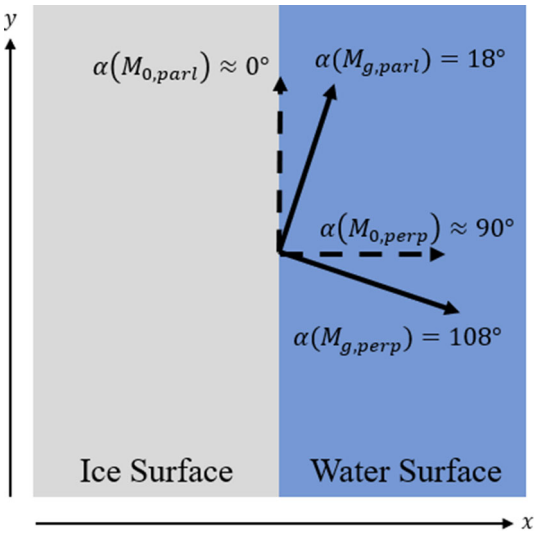


**Fig. 5** Birds-eye view of the imposed geostrophic ($M_g$) and the approximated surface ($M_0$) wind angles in the parallel and perpendicular configurations

## 5 The Combined Effects of $Ri_h$ and Wind Direction

In this section, we aim to understand the complexities added by varying the synoptic wind direction in the flow, while keeping the synoptic wind at a constant speed of 2 m s$^{-1}$. We thus design another suite of simulations where only $\Delta\theta_0$ is varied to vary $\mathrm{Ri}_h$, along with $\alpha$, to understand the dynamics and thermodynamics of the MIZ–ABL (Table 3). For each $\Delta\theta_0$, the wind angle $\alpha$ was changed to be either perpendicular or parallel to the ice/water coastline. The surface temperature is decreased or increased by 1 K for the ice and water surface, respectively, which thus increases $\Delta\theta_0$ by increments of 2 K, all the way up to $\Delta\theta_0 = 16$ K. See simulation information in Table 3.

Due to the presence of the Coriolis force, the geostrophic wind angle is aligned 18° to the right (clockwise) of the desired surface wind direction. The value of 18° is based on LES results from Ghannam and Bou-Zeid (2021) who examined the wind veer at various Rossby numbers using the same code. This is done such that the wind at the surface level is almost exactly parallel/perpendicular to the ice-water coastline (see Fig. 5). Due to the horizontally periodic domain, the surface wind in the perpendicular configuration would blow over an infinite pattern of ice patch then water patch, while in the parallel case, the surface wind blows along infinitely long strips of ice and water.

Since a different wind direction changes the dynamics (and thus thermodynamics) of the flow, it is preferable to attempt to scale both the perpendicular and parallel sets of Suite II separately. The perpendicular case retains its values of $m_{perp}$, $n_{perp}$, $p_{perp}$, and $q_{perp}$, but the parallel cases require new values of $m$, $n$, $p$, and $q$ (see Eqs. 12 and 13) for the ice and water surfaces, which we now denote with the $parl$ subscript. We thus repeated the process done for the Suite I and Suite II perpendicular ice case, searching for a linear fit between the external parameters modelled and internal/simulated heat flux values. For the ice surface, we obtained values for $m_{parl} = -1.41 \times 10^{-4}$ and $n_{parl}/m_{parl} = 0$, but Fig. 6a clearly indicates that a linear fit would be rather poor, and thus we do not attempt to propose or plot a scaling law for ice fluxes in the parallel wind case. However, one can notice that these fluxes over ice are very small in magnitude as the air travels continuously over the cold surface.

**Table 3** Suite II Simulation Details (all external variables except $\mathrm{Ri}_f$)

| Simulation | $\Delta\theta_0$ (K) | $\theta_{a,0}$ (K) | $\mathrm{Ri}_h$ | $\mathrm{Ri}_{f,perp}$ | $\mathrm{Ri}_{f,parl}$ |
|---|---|---|---|---|---|
| dT02-M02-perp, -parl | 2 | 270.2 | 18.1 | 0.022 | 0.047 |
| dT04-M02-perp, -parl | 4 | 270.4 | 36.2 | 0.028 | 0.094 |
| dT06-M02-perp, -parl | 6 | 270.6 | 54.2 | 0.033 | 0.126 |
| dT08-M02-perp, -parl | 8 | 270.8 | 72.3 | 0.048 | 0.153 |
| dT10-M02-perp, -parl | 10 | 271.0 | 90.3 | 0.086 | 0.207 |
| dT12-M02-perp, -parl | 12 | 271.2 | 108.2 | 0.106 | 0.265 |
| dT14-M02-perp, -parl | 14 | 271.4 | 126.2 | 0.149 | 0.332 |
| dT16-M02-perp, -parl | 16 | 271.6 | 144.1 | 0.223 | 0.402 |

Constants in this suite: Ro = 13.7, $f_c = 1.46 \times 10^{-4}$ Hz, $M_g = 2.0\,\mathrm{m\,s^{-1}}$

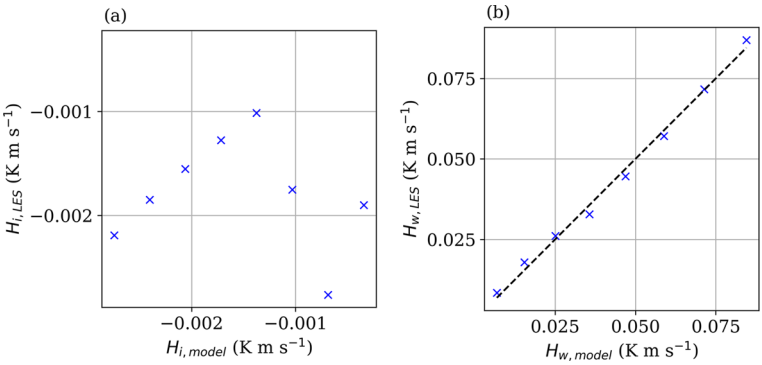


**Fig. 6** **a** Plot of modelled versus LES heat flux spatially-averaged over the ice surface, as in Eq. 19, for the parallel cases of Suite II (all cases have an $M_g = 2\,\mathrm{m\,s^{-1}}$). Here, $m_{parl} = -1.41 \times 10^{-4}$ and $n_{parl}/m_{parl} = 0$. **b** as in **a**, but for the water surface, following Eq. 20, where $p_{parl} = 2.96 \times 10^{-3}$ and $q_{parl}/p_{parl} = 0.1$

For such set-ups, the aggregate flux is fully dominated by the water surface for which the coefficient values $p_{parl} = 2.96 \times 10^{-3}$ and $q_{parl}/p_{parl} = 0.1$ provide a much better fit, with $R^2 = 0.998$. To first order, one can thus estimate $H_i \approx 0$. Figure 6 shows this scaling for these parallel cases of Suite II, which relate to the following equations:

$$H_{i,model} = a_i^2 \frac{\theta_r}{g z_i} M_g^3 m_{parl} \mathrm{Ri}_h \approx 0\,, \tag{19}$$

$$H_{w,model} = a_w^2 \frac{\theta_r}{g z_i} M_g^3 p_{parl} \left( \mathrm{Ri}_h + \frac{\mathrm{Ri}_h^{3/2}}{10} \right). \tag{20}$$

The vertical heat flux over the water surfaces in both parallel and perpendicular cases in Suites I and II (Figs. 4b and 6b) are very well approximated by the scaling model based solely on external simulation parameters. Over ice surfaces, the heat flux approximation in terms of $\mathrm{Ri}_h$ is adequate for perpendicular cases, but not for the parallel cases where these fluxes are minute due to weak turbulence as air continuously flows over ice (Figs. 4a and 6a). This can be explained by the differences in the dynamics of the flow. In the perpendicular cases (all of Suite I, and half of Suite II), air is constantly moving over both hot and cold patches (due to the periodicity of the domain). The air that reaches the ice patch is likely warmed up from the ocean and has high level of TKE. This allows the warm air to interact with the

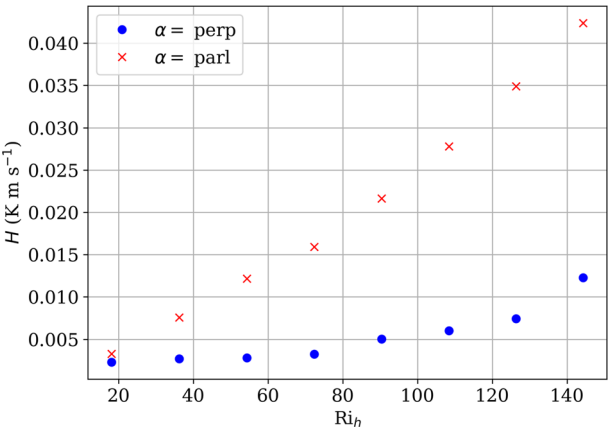


**Fig. 7** Surface heat flux $H$ (as computed by the LES, averaged over the entire heterogeneous surface) versus the heterogeneity Richardson number $\mathrm{Ri}_h$ for all Suite II cases. Blue dots correspond to perpendicular simulations; red crosses correspond to parallel simulations

ice, causing a strong negative heat flux, and thus a strong dependence on $\mathrm{Ri}_h$ that allows the model to perform well. However, in the parallel cases, wind at the surface flows parallel to the ice/water coastline. There is minimal mixing of air over the water surface interacting with the ice surface and this causes the air above the ice surface to adjust its temperature to be close to that of the ice surface, with strong and low turbulence levels. The resulting heat fluxes are thus very low and do not vary monotonically with $\mathrm{Ri}_h$ (though this may be due to insufficient statistical convergence for these small fluxes or to shortcomings related to insufficient LES grid resolution for this very stable part of the domain where turbulence may be intermittent (Shah and Bou-Zeid 2014; Allouche et al. 2022)).

The kinematic heat flux averaged over the whole surface, depicted in Fig. 7, clearly increases as $\mathrm{Ri}_h$ increases, which is to be expected since the buoyancy (driven by $\Delta\theta_0$) is increasing as well. However, this process seems to be 'damped' in the perpendicular case, again likely due to the constant exchange of cold air from the ice being pushed over the warmer sea surface and vice versa. This causes a significant fraction of the heat gained by the air over water to be returned to the surface over ice. This is minimized in the parallel case, where the fluxes over warm water are much larger than those over ice. For these parallel cases, it thus seems that the ice fluxes (which were poorly modelled by our scaling arguments) can be neglected at the regional aggregation scale.

One can decompose the surface heat flux into the friction velocity, $u_*$, and a surface-layer temperature scale $\theta_*$ following:

$$\overline{w'\theta'} = -\theta_* u_*, \tag{21}$$

where a prime denotes turbulent perturbation from the Reynolds average. This allows for determining whether or not mechanical forces or buoyancy explain the changes in the flow as $Ri_h$ changes. Both $u_*$ and $\overline{w'\theta'}$ were LES outputs, so $\theta_*$ was easily calculated. As $\mathrm{Ri}_h$ increases in both wind orientations, the increase in surface heat flux is predominantly attributed to the eddy temperature fluctuations $\theta_*$ in the surface layer, which is related to the increase in the surface temperature contrast (Fig. 8). This is expected since in this suite we modified $\mathrm{Ri}_h$ by changing $\Delta\theta_0$.

Since we can relate the kinematic heat flux over each surface to the external parameters, we can infer a flux heterogeneity Richardson number (based on either the LES or modelled

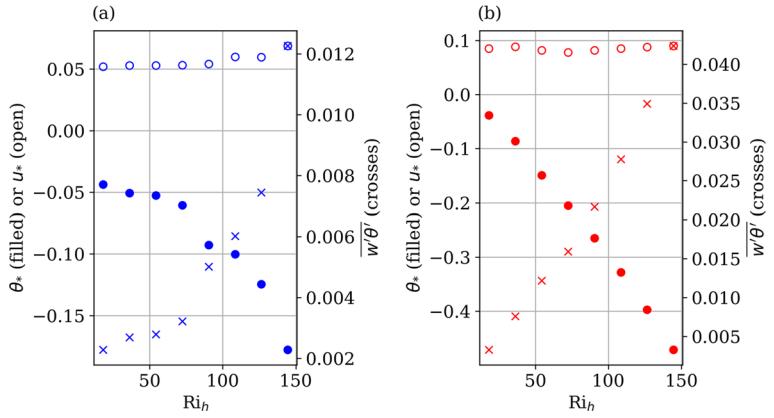


**Fig. 8** The decomposition of $\overline{w'\theta'}$ for the **a** perpendicular and **b** parallel cases in Suite II, averaged over the entire ice-water surface

values of $H_i$ and $H_w$), defined as:

$$\mathrm{Ri}_f = \frac{g}{\theta_r}\frac{H_w + H_i}{M_g^3/z_i}\,. \tag{22}$$

Note that since $H_i < 0$, the numerator is the difference of the fluxes' magnitude over the two surfaces. That is, it presumes that while the hot water patch injects mean kinetic energy (MKE) into the flow, the cold ice patch partially destroys that MKE and the two fluxes thus partially cancel each other dynamically. Ri$_f$ can be estimated using the general relationships for $H_i$ and $H_w$ in Eqs. 12 and 13 to create the general equation for relating Ri$_f$ to Ri$_h$:

$$\mathrm{Ri}_f = \mathrm{Ri}_h\left[a_w^2 p\left(1 + \frac{q}{p}\mathrm{Ri}_h^{1/2}\right) + a_i^2 m\left(1 + \frac{n}{m}\mathrm{Ri}_h^{1/2}\right)\right]. \tag{23}$$

Of course, the different wind directions have different physics, so a particular form for perpendicular (using Eqs. 12 and 13) and parallel (using Eqs. 19 and 20) wind directions, respectively, is provided below:

$$\mathrm{Ri}_{f,perp} = \mathrm{Ri}_h\left[a_w^2 p_{perp} + a_i^2 m_{perp}\left(1 - \frac{1}{4}\mathrm{Ri}_h^{1/2}\right)\right], \tag{24}$$

$$\mathrm{Ri}_{f,parl} = \mathrm{Ri}_h\left[a_w^2 p_{parl}\left(1 + \frac{1}{10}\mathrm{Ri}_h^{1/2}\right)\right]. \tag{25}$$

Note that the value of $H_i$ was set to 0 in the parallel case because its magnitude is negligible compared to $H_w$.

The relationship between Ri$_h$ and $Ri_f$ is good, with an $R^2$ value of 0.91 (Fig. 9). The imperfect and nonlinear scaling of Ri$_f$ with $Ri_h$ underlines the fact that temperature and flux contrasts are not identical or equivalent, and do not influence the flow in the same way. However, it does allow for an estimation of the temperature or heat flux $Ri$ from the other, which is useful since one of them is typically an external simulation input while the other is an internal output.

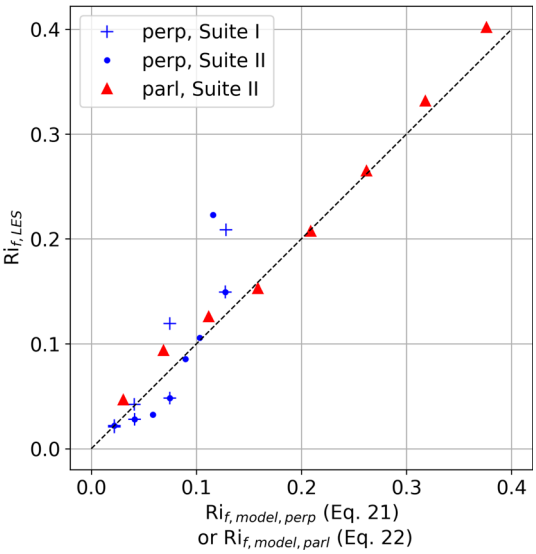


**Fig. 9** Testing the relationship between a model using $\mathrm{Ri}_h$ (among other external parameters) to $\mathrm{Ri}_f$, using the coefficients specific to each wind orientation. The $\mathrm{Ri}_f$ on the $y$-axis is comprised of the heat flux outputs as calculated by the LES. The expressions on the $x$-axis are calculated only using the external variables ($\mathrm{Ri}_h$, $a_i$, and $a_w$) and empirically-derived constants ($m_{perp}$, $p_{perp}$, and $p_{parl}$)

## 6 Turbulent and Dispersive Fluxes and Secondary Circulations

To further explain the impact of $Ri_h$ and $\alpha$ on surface heat fluxes and examine their effect on the larger scale flow in the ABL, in this section, we consider the flow structures and how they modulate dispersive and turbulent fluxes. The temperature heterogeneity of the surface will induce secondary circulations that bring about dispersive fluxes in a horizontal plane, which can represent a significant contribution to the total momentum or scalar transfer. These dispersive fluxes emerge in a time-averaged but spatially-variable mean flow (Raupach and Shaw 1982; Li and Bou-Zeid 2019). Since our Reynolds averaging is done in time and $y$, we can spatially decompose a Reynolds-averaged variable following $\overline{w} = \langle \overline{w} \rangle + \overline{w}''$, where the brackets represent the spatial average (as defined in Sect. 3) and the double-prime represents the perturbation of the mean fields in space. We then calculate the dispersive fluxes, for heat for example, by:

$$\overline{w}\overline{\theta} = \left(\langle \overline{w} \rangle + \overline{w}''\right)\left(\langle \overline{\theta} \rangle + \overline{\theta}''\right) = \overline{w}''\langle \overline{\theta} \rangle + \overline{w}''\overline{\theta}''. \tag{26}$$

Here, $\langle \overline{w} \rangle$ is assumed to be very small (unless strong and large scale subsidence or uplift are present); in our LES it has to be identically zero since there cannot be accumulation or depletion of mass below a given horizontal plane in a periodic domain with an incompressible flow. While the first term on the right hand side is not zero locally and contributes to local fluxes, its spatial average $\langle \overline{w}''\langle \overline{\theta} \rangle \rangle = \langle \overline{w}'' \rangle \langle \overline{\theta} \rangle = 0$ since $\langle \overline{w}'' \rangle = 0$ by definition; therefore, this term has no impact on spatially-averaged surface-atmosphere exchanges. The second term is of most interest: $\overline{w}''\overline{\theta}''$ is the dispersive flux, a spatial correlation between regions with consistent structures (such as consistent warm updrafts or cool downdrafts). It is worth noting that the dispersive flux of heat is also directly related to the buoyancy generation of MKE, $(g/\theta_r)(\overline{w}\hat{\overline{\theta}})$. In our LES, since we use the planar mean of the potential temperature as the Boussinesq reference, we further have $\theta_r = \langle \theta \rangle$ and $\hat{\overline{\theta}} = \overline{\theta}''$. With $\langle \overline{w} \rangle = 0$, $\overline{w}'' = \overline{w}$ and thus $\overline{w}\hat{\overline{\theta}} = \overline{w}''\overline{\theta}''$. That is, the buoyancy production of the MKE that results in the secondary circulations is directly proportional to the dispersive heat flux.

The structure of the resulting secondary circulations has a significant impact on fluxes and wind profiles in the MIZ–ABL, as seen in the heat flux and streamlines plots of Figs. 10 and 11. In the perpendicular cases, the IBL is modulated by the circulation. As $\mathrm{Ri}_h$ increases (from top to bottom) in this case, the IBL loses its coherence and becomes shallower as buoyant forcing overcomes the geostrophic forcing. The turbulent and dispersive heat flux magnitudes increase over the entire domain. The streamlines change moderately as $\Delta\theta_0$ increases from the dT02-perp to the dT08-perp simulations: they maintain their left-to-right flow driven by the synoptic wind forcings. However, in the dT16-perp simulation, a circulation develops over the cold surface, likely due to the convergence zone that would normally lie over the hot patch but that here is pushed downstream by the geostrophic wind. In this case, the dispersive fluxes are of comparable magnitude to the turbulent ones.

For the parallel cases, the heat fluxes are overall stronger than in the perpendicular case and mostly positive since the flux over ice is very small as previously discussed (compare the colourbars of the two figures). The dispersive fluxes are comparable to the turbulent ones for all temperature contrasts, and their heat flux extends much higher into the atmosphere over the warm patch. These results are due to the minimal interaction between air over the water surface and air over the ice surface, which allows the secondary circulations to strengthen considerably relative to the perpendicular simulations.

Dynamically, as $\mathrm{Ri}_h$ increases in the parallel simulations, the streamlines rapidly evolve from a weak left-to-right wind in the dT02-M02-parl case (remember that in these cases, the geostrophic wind is going into the figure as displayed in 5), to strong thermal rolls in the dT16-M02-parl case (Fig. 11). These rolls develop in the presence of a weak geostrophic forcing due to the so-called thermal torque as explained in Bou-Zeid et al. (2020), which results in the buoyant production of MKE discussed earlier in this section. This thermal torque is what gives the parallel case, where the geostrophic wind does not oppose secondary structures, a higher TKE than the perpendicular case,where the secondary structures are weakened by the geostrophic wind (TKE results not shown). These rolls have been seen in other heterogeneous surfaces, such as over patches of different roughness lengths (Anderson et al. 2015). One gap in our study regarding the secondary circulations occurs as the geostrophic wind transitions from perpendicular to parallel flow (referred to as *oblique flow*). It has been reported that flow will transition abruptly at some point between perpendicular and parallel flow regimes when driven by different surface roughness lengths (Anderson 2020), but more studies are needed on oblique flow for thermally heterogeneous surfaces.

The secondary circulations explored in the previous section bring about dispersive fluxes by inducing a mean upward or downward advective flux. Figures 10 and 11 show the $x$-$z$ planes of the dT02, dT08, and dT16 simulations for the dispersive heat flux. These consistent structures form as $\mathrm{Ri}_h$ increases due to the increase of buoyant MKE generation over the relatively warmer water. This disrupts the IBL in the perpendicular case, while strengthening the secondary motions (most notably, the consistently warm updraft over the water surface) in the parallel case.

In the perpendicular case, as $\mathrm{Ri}_h$ increases, these dispersive fluxes get stronger and more concentrated near the surface, increasing the magnitude of surface-air interactions (Fig. 10). Here, the dispersive-to-turbulent flux ratio increases with $\mathrm{Ri}_h$, from $\mathcal{O}(\times 10^{-2})$ in DT02 to $\mathcal{O}(1)$ in DT16. Dispersive-to-turbulent ratios of $\mathcal{O}(1)-\mathcal{O}(\times 10^{-1})$ have also been reported for heterogeneous flat surfaces (Margairaz et al. 2020) and for flows over urban canopies (Li and Bou-Zeid 2019; Blunn et al. 2022)). In the parallel case, these dispersive fluxes are already stronger even at low $\mathrm{Ri}_h$, due to the structure of the secondary circulations, so the dispersive-to-turbulent flux ratio for all three cases is of $\mathcal{O}(\times 10^{-1})$. Since there is minimal interaction between air over the two different types of surfaces, the dispersive fluxes concentrate more

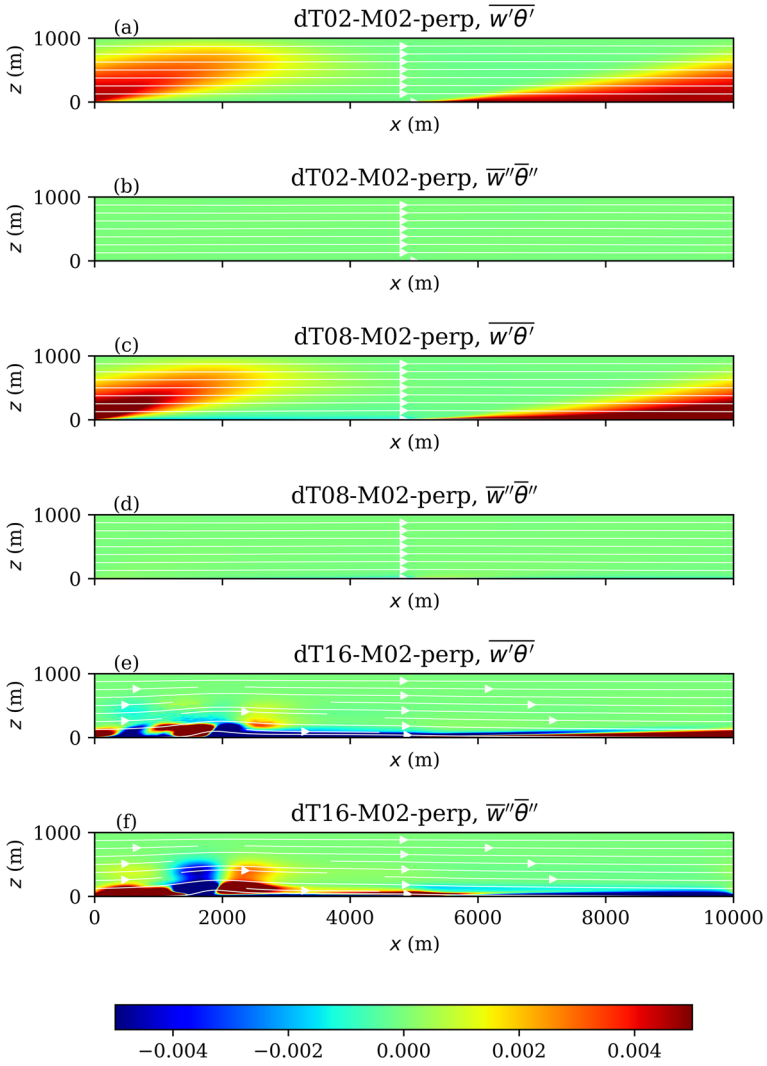


**Fig. 10** Turbulent ($\overline{w'\theta'}$) and dispersive ($\overline{w}''\,\overline{\theta}''$) heat flux (K m s$^{-1}$) overlaid with ($u$, $w$) streamlines for dT02-M02-perp, dT08-M02-perp, and dT16-M02-perp. Geostrophic wind flows left-to-right. All variables with an overbar are Reynolds-averaged in time and the $y$ direction (as there is no heterogeneity in the $y$-direction, see Fig. 5). Ice surface is on the left half of the plot, with water surface on the right half

over the warm surface (Fig. 11), so there is certainly a spatial variability component to the turbulent-to-dispersive ratios.

## 7 Conclusions

The overarching goal of the paper is to elucidate the scaling, dynamics, and surface-air interactions in the MIZ–ABL. Two suites of LES runs were used to address the four scientific questions formulated in the introduction, and here we present a synthesis of the findings to provide the answers.

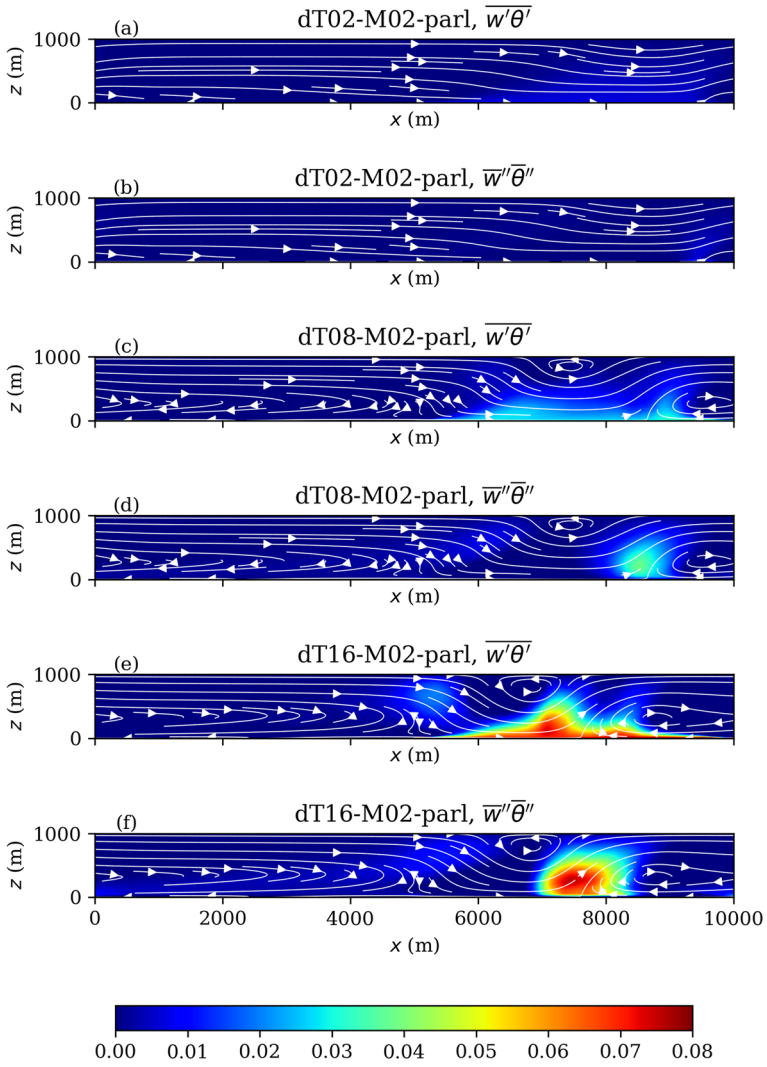


**Fig. 11** Turbulent ($\overline{w'\theta'}$) and dispersive ($\overline{w}''\overline{\theta}''$) heat flux (K m s$^{-1}$) overlaid with ($u$, $w$) streamlines for dT02-M02-parl, dT08-M02-parl, and dT16-M02-parl. Geostrophic wind flows into the page. All variables with an overbar are Reynolds-averaged in time and the $y$ direction (as there is no heterogeneity in the $y$-direction, see Fig. 5). Ice surface is on the left half of the plot, with water surface on the right half

Question 1: What scaling can capture the competing effects of buoyant circulations and synoptic forcing to provide a unifying framework for understanding the dynamics and thermodynamics of the heterogeneous MIZ–ABL? In Sect. 2, we proposed a framework for non-dimensionalizing the geometry and dynamics of the MIZ–ABL problem. The framework was minimal in the sense that we only included the parameters that are highly likely to be consequential. The present paper focused on testing two dimensionless groups that represented the dynamics, while those representing the geometry were kept fixed. The geostrophic wind angle relative to the surface was one of these dynamical groups, and indeed the results

of the paper confirm that it has a significant impact on the results. The second dimensionless group was formulated as a heterogeneity Richardson number, $\mathrm{Ri}_h$, that compared the effect buoyant circulations driven by the surface temperature contrast to the geopstrophic forcing that causes advection and mechanical shear. This number was also found to be necessary for scaling the dynamics, but it does not seem to be sufficient. The results were sensitive to this Richardson number, but simulations with similar $\mathrm{Ri}_h$ did not always yield identical normalized results. $\mathrm{Ri}_h$ attempts to combine the stability over the ice and that over water into a single group, postulating that only the difference in stability is relevant to the dynamics. The results, however, indicate that perfect similarity may require one additional dimensionless group to represent atmospheric stability over one of the surfaces (the stability over the other surface then becomes deducible from that new group and $\mathrm{Ri}_h$), or equivalently, two classical Richardson numbers for the two surfaces. The need for two dimensionless groups is supported by similar work on urban-rural circulations (Omidvar et al. 2020).

Nevertheless, the present results indicate that the simple approach with one dimensionless group tested here may give acceptable results for surface heat fluxes (but not for the ABL flow and turbulence). This is quite useful since it allows, knowing the value of $\mathrm{Ri}_h$ and wind angle prior to running a simulation on in a coarse weather or climate model, to estimate the heat flux. The effect of heterogeneity patterns and geometry, however, requires further investigation.

Question 2: How do the mean wind profile, TKE, and surface fluxes respond to an increase in the surface temperature difference $\Delta\theta_0$ between ice and water? For a constant wind direction perpendicular to the water-ice interface, and at lower values of $\mathrm{Ri}_h$, the mechanical forcing dominates the dynamics: the profiles of wind and TKE collapse when normalized by $M_g$. When $\mathrm{Ri}_h$ increases, the results normalized by $M_g$ diverge as buoyancy effects become prominent. With an increase in the surface temperature contrast and $\mathrm{Ri}_h$, the wind profiles display increasing shear as a result of the secondary circulations, while the TKE, normalized by $M_g^2$ increases. Both the mean wind and TKE decrease when normalized by the buoyant velocity scale $W_b$, indicating that an increase in the thermal surface contrast does not result in a proportional increase in the turbulent kinetic energy in the MIZ–ABL. This is explained by the fact that most of the buoyant energy production ends up in the MKE of the secondary circulations, rather than in the TKE budget. The surface heat fluxes over ice, sea, and the total aggregate surface generally increase with $\mathrm{Ri}_h$, as expected, regardless of wind direction. According to the scaling that we propose and test, the positive fluxes over the water surface increase proportionally to $\mathrm{Ri}_h$ and hence to $\Delta\theta_0$, while the negative fluxes over ice seem to increase with $\mathrm{Ri}_h^{3/2}$. The faster-than-linear scaling over ice can be explained by the increased wind speed and turbulence over the colder surface, reducing local stability, as secondary circulations increase for the perpendicular case.

Question 3: What is the effect of the orientation of the surface patterns relative to the wind direction $\alpha$? The effect of wind direction, as our results indicate, is critical especially when studying the secondary circulations produced by the combination of wind and thermal contrast. In perpendicular cases, the wind direction acts as a sort of "damping" on the total heat flux as positive ocean-to-atmosphere fluxes are partially compensated by negative atmosphere-to-ice fluxes. The constant change in heat flux breaks down any coherent structures that tend to form, favouring the development of internal and equilibrium boundary layers that maintain significant turbulence over ice despite the locally-strong temperature gradient. By contrast, in the parallel cases, when wind flows along an ice-water coastline for a very long time (due to the periodic nature of the LES ), the heat injection into the atmo-

sphere is larger and more intense over the ocean because there are secondary circulations advecting cold air near the surface from ice to water. These circulations, however, do not convey much turbulence as they descend over the ice and bring only weakly turbulent air from aloft, resulting in weak negative fluxes over ice. A weighted average approach would erroneously yield equivalent impacts for an ice fraction of $f_i = 0.5$, so a new parameter that accounts for the asymmetry in fluxes based on $\alpha$ should be used to determine how the buoyant and mechanical forces interact with one another, and that can change depending on the ice surface pattern itself. Real-world ice maps, most often, will feature a combination of parallel, perpendicular and oblique interfaces; and our results indicate that this information, and any preferential orientation, should be accounted for in parameterizations for coarse models.

Question 4: How do $\Delta\theta_0$ and $\alpha$ combine to set up secondary circulations and modulate the turbulent and dispersive exchanges of heat and momentum in the MIZ–ABL? The secondary circulations set up by these parameters increase in intensity as $\mathrm{Ri}_h$ increases, and developing scaling laws for these higher-order fluxes becomes more difficult with a single non-dimensional parameter to characterize buoyancy effects in the domain. For parallel cases, the secondary circulations are not hindered by the geostrophic forcing and display vigorous activity. In contrast, for the perpendicular cases, internal boundary layers dominate at low $\mathrm{Ri}_h$, giving way to secondary circulations oriented parallel to the shore only at the higher $\mathrm{Ri}_h$ we simulate. These circulations, however, remain weaker than for parallel winds.

As stressed before, more investigations are required to (i) understand how the heterogeneity parameter, $l_h$, affects the flow, (ii) examine how these idealized flow features behave over real ice maps, and (iii) examine what additional dimensionless groups can be added to complete the similarity framework for the flow dynamics, among other questions that remain unanswered.

**Acknowledgements** This research was supported by the US National Science Foundation under award number AGS 2128345 and the National Oceanic and Atmospheric Administration, U.S. Department of Commerce under by award NA18OAR4320123. The statements, findings, conclusions, and recommendations are those of the authors and do not necessarily reflect the views of the National Oceanic and Atmospheric Administration, or the U.S. Department of Commerce. We would also like to acknowledge high-performance computing support from Cheyenne (Computational and Information Systems Laboratory 2019) provided by NCAR's Computational and Information Systems Laboratory, sponsored by the National Science Foundation, under projects UPRI0007 and UPRI0021.

**Data Availability** The dataset on these half-and-half ice/water surfaces are publicly available at http://arks.princeton.edu/ark:/88435/dsp01rv042x315.

## References

Allouche M, Katul GG, Fuentes JD, Bou-Zeid E (2021) Probability law of turbulent kinetic energy in the atmospheric surface layer. Phys Rev Fluids 6(074):601. https://doi.org/10.1103/PhysRevFluids.6.074601

Allouche M, Bou-Zeid E, Ansorge C, Katul GG, Chamecki M, Acevedo O, Thanekar S, Fuentes JD (2022) The detection, genesis, and modeling of turbulence intermittency in the stable atmospheric surface layer. J Atmos Sci 79(4):1171–1190. https://doi.org/10.1175/JAS-D-21-0053.1

Anderson W (2020) Turbulent channel flow over heterogeneous roughness at oblique angles. J Fluid Mech 886:A15. https://doi.org/10.1017/jfm.2019.1022

Anderson W, Barros JM, Christensen KT, Awasthi A (2015) Numerical and experimental study of mechanisms responsible for turbulent secondary flows in boundary layer flows over spanwise heterogeneous roughness. J Fluid Mech 768:316–347. https://doi.org/10.1017/jfm.2015.91

Baidya Roy S (2002) Impact of land use/land cover change on regional hydrometeorology in Amazonia. J Geophys Res 107(D20):8037. https://doi.org/10.1029/2000JD000266

Bates NR, Moran SB, Hansell DA, Mathis JT (2006) An increasing $CO_2$ sink in the Arctic Ocean due to sea-ice loss. Geophys Res Lett 33(23):L23,609. https://doi.org/10.1029/2006GL027028

Blunn LP, Coceal O, Nazarian N, Barlow JF, Plant RS, Bohnenstengel SI, Lean HW (2022) Turbulence characteristics across a range of idealized urban canopy geometries. Boundary-Layer Meteorol 182(2):275–307. https://doi.org/10.1007/s10546-021-00658-6

Bou-Zeid E, Meneveau C, Parlange MB (2004) Large-eddy simulation of neutral atmospheric boundary layer flow over heterogeneous surfaces: blending height and effective surface roughness. Water Resour Res 40(W02):505. https://doi.org/10.1029/2003WR002475

Bou-Zeid E, Meneveau C, Parlange M (2005) A scale-dependent Lagrangian dynamic model for large eddy simulation of complex turbulent flows. Phys Fluids 17(2):025,105. https://doi.org/10.1063/1.1839152

Bou-Zeid E, Parlange MB, Meneveau C (2007) On the parameterization of surface roughness at regional scales. J Atmos Sci 64(1):216–227. https://doi.org/10.1175/JAS3826.1

Bou-Zeid E, Higgins C, Huwald H, Meneveau C, Parlange MB (2010) Field study of the dynamics and modelling of subgrid-scale turbulence in a stable atmospheric surface layer over a glacier. J Fluid Mech 665:480–515. https://doi.org/10.1017/S0022112010004015

Bou-Zeid E, Anderson W, Katul GG, Mahrt L (2020) The persistent challenge of surface heterogeneity in boundary-layer meteorology: a review. Boundary-Layer Meteorol 177(2–3):227–245. https://doi.org/10.1007/s10546-020-00551-8

Bourassa MA, Gille ST, Bitz C, Carlson D, Cerovecki I, Clayson CA, Cronin MF, Drennan WM, Fairall CW, Hoffman RN, Magnusdottir G, Pinker RT, Renfrew IA, Serreze M, Speer K, Talley LD, Wick GA (2013) High-latitude ocean and sea ice surface fluxes: challenges for climate research. Bull Am Meteorol Soc 94(3):403–423. https://doi.org/10.1175/BAMS-D-11-00244.1

Bradley EF (1968) A micrometeorological study of velocity profiles and surface drag in the region modified by a change in surface roughness. Q J R Metorol Soc 94(401):361–379. https://doi.org/10.1002/qj.49709440111

Bradshaw P, Huang GP (1995) The law of the wall in turbulent flow. Proc Math Phys Sci 451(1941):165–188

Brutsaert W (2005) Hydrology: an introduction. Cambridge University Press, Cambridge

Chechin DG, Makhotina IA, Lüpkes C, Makshtas AP (2019) Effect of wind speed and leads on clear-sky cooling over arctic sea ice during polar night. J Atmos Sci 76(8):2481–2503. https://doi.org/10.1175/JAS-D-18-0277.1

Claussen M (1991) Local advection processes in the surface layer of the marginal ice zone. Boundary-Layer Meteorol 54(1–2):1–27. https://doi.org/10.1007/BF00119409

Computational and Information Systems Laboratory (2019) Cheyenne: HPE/SGI ICE XA System (University Community Computing). Boulder, CO: National Center for Atmospheric Research. https://doi.org/10.5065/D6RX99HX

Courault D, Drobinski P, Brunet Y, Lacarrere P, Talbot C (2007) Impact of surface heterogeneity on a buoyancy-driven convective boundary layer in light winds. Boundary-Layer Meteorol 124(3):383–403. https://doi.org/10.1007/s10546-007-9172-y

Esau IN (2007) Amplification of turbulent exchange over wide Arctic leads: large-eddy simulation study. J Geophys Res 112(D8):D08,109. https://doi.org/10.1029/2006JD007225

Fiedler EK, Lachlan-Cope TA, Renfrew IA, King JC (2010) Convective heat transfer over thin ice covered coastal polynyas. J Geophys Res 115(C10):2009JC005,797. https://doi.org/10.1029/2009JC005797

Ghannam K, Bou-Zeid E (2021) Baroclinicity and directional shear explain departures from the logarithmic wind profile. Q J R Meteorol Soc 147(734):443–464. https://doi.org/10.1002/qj.3927

Hall D, Key J, Case K, Riggs G, Cavalieri D (2004) Sea ice surface temperature product from MODIS. IEEE Trans Geosci Remote Sens 42(5):1076–1087. https://doi.org/10.1109/TGRS.2004.825587

Huang HY, Margulis SA, Chu CR, Tsai HC (2011) Investigation of the impacts of vegetation distribution and evaporative cooling on synthetic urban daytime climate using a coupled LES-LSM model. Hydrol Process 25(10):1574–1586. https://doi.org/10.1002/hyp.7919

Huang J, Bou-Zeid E (2013) Turbulence and vertical fluxes in the stable atmospheric boundary layer. part i: a large-eddy simulation study. J Atmos Sci 70(6):1513–1527. https://doi.org/10.1175/JAS-D-12-0167.1

Khvorostyanov VI, Curry JA, Gultepe I, Strawbridge K (2003) A springtime cloud over the Beaufort Sea polynya: three-dimensional simulation with explicit spectral microphysics and comparison with observations: simulation of cloud over polynya. J Geophys Res. https://doi.org/10.1029/2001JD001489

Kleissl J, Kumar V, Meneveau C, Parlange MB (2006) Numerical study of dynamic Smagorinsky models in large-eddy simulation of the atmospheric boundary layer: validation in stable and unstable conditions. Water Resour Res. https://doi.org/10.1029/2005WR004685

Kumar V, Kleissl J, Meneveau C, Parlange MB (2006) Large-eddy simulation of a diurnal cycle of the atmospheric boundary layer: Atmospheric stability and scaling issues: LES of a diurnal cycle of the ABL. Water Resour Res. https://doi.org/10.1029/2005WR004651

Li D, Bou-Zeid E, Barlage M, Chen F, Smith JA (2013) Development and evaluation of a mosaic approach in the WRF-NOAH framework. J Geophys Res Atmos 118:11,918-11,935. https://doi.org/10.1002/2013JD020657

Li Q, Bou-Zeid E (2019) Contrasts between momentum and scalar transport over very rough surfaces. J Fluid Mech 880:32–58. https://doi.org/10.1017/jfm.2019.687

Li Q, Bou-Zeid E, Anderson W, Grimmond S, Hultmark M (2016) Quality and reliability of LES of convective scalar transfer at high Reynolds numbers. Int J Heat Mass Transf 102:959–970. https://doi.org/10.1016/j.ijheatmasstransfer.2016.06.093

Liu Y, Key JR, Liu Z, Wang X, Vavrus SJ (2012) A cloudier Arctic expected with diminishing sea ice: cloudier arctic with diminishing sea ice. Geophys Res Lett. https://doi.org/10.1029/2012GL051251

Lüpkes C, Birnbaum G (2005) Surface drag in the arctic marginal sea-ice zone: a comparison of different parameterisation concepts. Boundary-Layer Meteorol 117(2):179–211. https://doi.org/10.1007/s10546-005-1445-8

Mahrt L, Bou-Zeid E (2020) Non-stationary boundary layers. Boundary-Layer Meteorol 177(2–3):189–204. https://doi.org/10.1007/s10546-020-00533-w

Margairaz F, Pardyjak ER, Calaf M (2020) Surface thermal heterogeneities and the atmospheric boundary layer: the thermal heterogeneity parameter. Boundary-Layer Meteorol 177(1):49–68. https://doi.org/10.1007/s10546-020-00544-7

Maronga B, Raasch S (2013) Large-Eddy simulations of surface heterogeneity effects on the convective boundary layer during the LITFASS-2003 experiment. Boundary-Layer Meteorol 146(1):17–44. https://doi.org/10.1007/s10546-012-9748-z

Momen M, Bou-Zeid E (2016) Large-eddy simulations and damped-oscillator models of the unsteady ekman boundary layer*. J Atmos Sci 73:25–40. https://doi.org/10.1175/JAS-D-15-0038.1

Momen M, Bou-Zeid E (2017) Mean and turbulence dynamics in unsteady Ekman boundary layers. J Fluid Mech 816:209–242. https://doi.org/10.1017/jfm.2017.76

Morrison T, Calaf M, Higgins CW, Drake SA, Perelet A, Pardyjak E (2021) The impact of surface temperature heterogeneity on near-surface heat transport. Boundary-Layer Meteorol 180(2):247–272. https://doi.org/10.1007/s10546-021-00624-2

Omidvar H, Bou-Zeid E, Li Q, Mellado JP, Klein P (2020) Plume or bubble? Mixed-convection flow regimes and city-scale circulations. J Fluid Mech 897:A5. https://doi.org/10.1017/jfm.2020.360

Orszag SA (1971) On the elimination of aliasing in finite-difference schemes by filtering high-wavenumber components. J Atmos Sci 28:1074

Palm SP, Strey ST, Spinhirne J, Markus T (2010) Influence of Arctic sea ice extent on polar cloud fraction and vertical structure and implications for regional climate. J Geophys Res 115(D21):D21,209. https://doi.org/10.1029/2010JD013900

Pithan F, Ackerman A, Angevine WM, Hartung K, Ickes L, Kelley M, Medeiros B, Sandu I, Steeneveld GJ, Sterk HAM, Svensson G, Vaillancourt PA, Zadra A (2016) Select strengths and biases of models in representing the Arctic winter boundary layer over sea ice: the Larcform 1 single column model intercomparison: FIRST ARCTIC AIR MASS INTERCOMPARISON. J Adv Model Earth Syst 8(3):1345–1357. https://doi.org/10.1002/2016MS000630

Raddatz RL, Papakyriakou TN, Else BG, Swystun K, Barber DG (2015) A simple scheme for estimating turbulent heat flux over landfast arctic sea ice from dry snow to advanced melt. Boundary-Layer Meteorol 155(2):351–367. https://doi.org/10.1007/s10546-014-0002-8

Raupach MR, Shaw RH (1982) Averaging procedures for flow within vegetation canopies. Bound-Layer Meteorol 22:79–90. https://doi.org/10.1007/BF00128057

Rosenblum E, Eisenman I (2016) Faster arctic sea ice retreat in CMIP5 than in CMIP3 due to volcanoes. J Clim 29(24):9179–9188. https://doi.org/10.1175/JCLI-D-16-0391.1

Shah SK, Bou-Zeid E (2014) Direct numerical simulations of turbulent Ekman layers with increasing static stability: modifications to the bulk structure and second-order statistics. J Fluid Mech 760:494–539. https://doi.org/10.1017/jfm.2014.597

Stoll R, Gibbs JA, Salesky ST, Anderson W, Calaf M (2020) Large-eddy simulation of the atmospheric boundary layer. Boundary-Layer Meteorol 177(2–3):541–581. https://doi.org/10.1007/s10546-020-00556-3

Stroeve J, Holland MM, Meier W, Scambos T, Serreze M (2007) Arctic sea ice decline: faster than forecast. Geophys Res Lett. https://doi.org/10.1029/2007GL029703

Strong C, Foster D, Cherkaev E, Eisenman I, Golden KM (2017) On the definition of marginal ice zone width. J Atmos Oceanic Technol 34(7):1565–1584. https://doi.org/10.1175/JTECH-D-16-0171.1

Taylor P, Hegyi B, Boeke R, Boisvert L (2018) On the increasing importance of air-sea exchanges in a thawing arctic: a review. Atmosphere 9(2):41. https://doi.org/10.3390/atmos9020041

Townsend AA (1961) Equilibrium layers and wall turbulence. J Fluid Mech 11(1):97–120. https://doi.org/10.1017/S0022112061000883

Tseng YH, Meneveau C, Parlange MB (2006) Modeling flow around bluff bodies and predicting urban dispersion using large eddy simulation. Environ Sci Technol 40(8):2653–2662. https://doi.org/10.1021/es051708m

Untersteiner N, Badgley FI (1965) The roughness parameters of sea ice. J Geophys Res 70(18):4573–4577. https://doi.org/10.1029/JZ070i018p04573

Vihma T (1995) Subgrid parameterization of surface heat and momentum fluxes over polar oceans. J Geophys Res 100(C11):22,625. https://doi.org/10.1029/95JC02498

Wenta M, Herman A (2019) Area-averaged surface moisture flux over fragmented sea ice: floe size distribution effects and the associated convection structure within the atmospheric boundary layer. Atmosphere 10(11):654. https://doi.org/10.3390/atmos10110654

Willingham D, Anderson W, Christensen KT, Barros JM (2014) Turbulent boundary layer flow over transverse aerodynamic roughness transitions: Induced mixing and flow characterization. Phys Fluids 26(2):025,111. https://doi.org/10.1063/1.4864105

Zahn E, Bou-Zeid E, Dias NL (2023) Relaxed eddy accumulation outperforms Monin–Obukhov flux models under non-ideal conditions. Geophys Res Lett. https://doi.org/10.1029/2023GL103099